

A PeVatron Candidate: Modeling the Boomerang Nebula in X-ray Band

Xuan-Han Liang,* Chao-Ming Li, Qi-Zuo Wu, Jia-Shu Pan and Ruo-Yu Liu

Department of Astronomy, Nanjing University, 163 Xianlin Avenue, Nanjing 210023, China

Key Laboratory of Modern Astronomy and Astrophysics, Nanjing University, Ministry of Education, Nanjing 210023, China

E-mail: xhliang@smail.nju.edu.cn, mg21260008@smail.nju.edu.cn,

qzwu@smail.nju.edu.cn, 181830148@smail.nju.edu.cn, ryliu@nju.edu.cn

Pulsar wind nebula (PWN) Boomerang and the associated supernova remnant (SNR) G106.3+2.7 are among candidates for the ultra-high-energy (UHE) gamma-ray counterparts published by LHAASO. Although the centroid of the extended source, LHAASO J2226+6057, deviates from the pulsar's position by about 0.3° , the source partially covers the PWN. Therefore, we cannot totally exclude the possibility that part of the UHE emission comes from the PWN. Indeed, recent gamma-ray analyses by MAGIC and HAWC do separate two sources associated with the PWN and the SNR. Previous studies mainly focus on whether the SNR is a PeVatron, while neglecting the energetic PWN. Here, we explore the possibility of the Boomerang Nebula being a PeVatron candidate by studying its X-ray radiation. By modeling the diffusion of relativistic electrons injected in the PWN, we fit the radial profiles of X-ray surface brightness and photon index. The solution with a magnetic field $B = 140 \mu\text{G}$ can well reproduce the observed profiles and implies a severe suppression of IC scattering of electrons. Hence, we propose to introduce a proton component to account for the UHE emission partly originating from the PWN in light of the LHAASO measurement on Crab. In this sense, Boomerang Nebula would be a hadronic PeVatron. Longer detection time of LHAASO may be helpful for verifying the hypothesis.

38th International Cosmic Ray Conference (ICRC2023)
26 July - 3 August, 2023
Nagoya, Japan



*Speaker

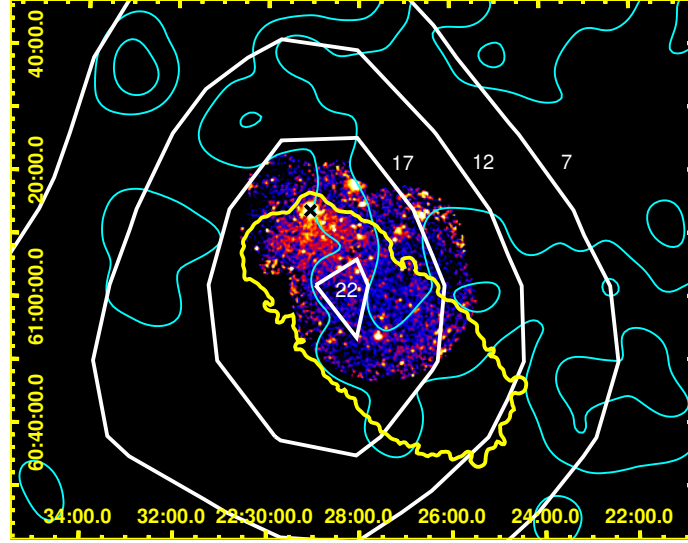


Figure 1: Observation results from different energy bands in equatorial coordinate system. The central-colored part is the combination of the X-ray observation from Chandra and XMM-Newton (5). The pulsar position is marked with a black cross. The yellow curve outlines the 1.4 GHz radio continuum of the SNR (2). The cyan contours show the CO emission of the molecular cloud (3). The white contours show the LHAASO observation with numbers representing \sqrt{TS} values (1).

1. Boomerang Nebula

The galactic sources that can accelerate cosmic rays (CRs) to PeV regime are called PeVatrons. The twelve ultra-high-energy (UHE, $E_\gamma > 100$ TeV) gamma-ray sources published by LHAASO has caught much attention from the community as they are long-sought PeVatron candidates (1). LHAASO J2226+6057 is among the twelve sources and has been intensively studied with multi-wavelength data. We summarize the observations including X-ray, LHAASO and CO for reference in Figure 1. Due to the complexity of the source, the origin of the UHE gamma-ray remains unclear. One possible counterpart is the elongated SNR G106.3+2.7, which can be divided into two distinct components according to the radio observation, the compact bright "head" region and the diffuse faint "tail" region (2). The former is located in the northeast of the comet-shaped structure, while the latter extends to the southwest and is believed to break into a large low-density HI bubble (3). The most prominent structure of the head region is the Boomerang Nebula in the north, which is another possible origin of energetic CRs and powered by the pulsar PSR J2229+6114 with a characteristic age of 10 kyr. The location of the molecular clouds found in the PWN-SNR complex seems to be coincident with the tail region in our line of sight based on CO observations (3), but it is still uncertain whether the molecular clouds are directly disturbed by the SNR shocks (4). Nevertheless, they are expected to be nearby and can be illuminated by the protons escaped from the SNR (5, 6).

Another key question is whether the origin of the UHE emission is leptonic or hadronic. One way to find out is to fit the gamma-ray spectrum with data from GeV to TeV including Fermi-LAT (7, 8), Milagro (9, 10), MAGIC (11), VERITAS (12), HAWC (13) Tibet AS γ (14) and LHAASO (1). The hadronic origin of the TeV photons is favored because of the spacial coincidence between the extended gamma-ray emission and the molecular clouds in the tail region (e.g., (5, 14)). However,

the extended LHAASO source partially covers the head region and thus the possibility of PWN being a PeVatron cannot be ruled out. Recent analyses from MAGIC and HAWC manage to separate two sources corresponding to head and tail and we expect the similar attempt from LHAASO.

On the other hand, X-ray data suggest a nonthermal origin (5, 15) and provide an approach to estimate the magnetic field. Ge et al. (5) (hereafter Ge2021) obtained radial profiles of X-ray intensity and photon index as a function of the distance from the pulsar and suggested two different origins of the electrons, namely the PWN and the SNR. To test this hypothesis and evaluate the magnetic field, we model the X-ray profiles around the Boomerang Nebula with diffusing relativistic electrons injected in the PWN.

2. X-ray Profiles

We consider two electron components in our simulations according to Ge2021. With the electron distribution, we can calculate the X-ray emission at 1–7 keV and integrate the emission along the line of sight to get the intensity. The best-fit result can be obtained using MCMC by comparing the derived profiles of intensity and photon index with the observed one.

For the SNR-accelerated electrons, we directly adopt the fitting results corresponding to a uniform electron distribution in the range of 600 arcmin² of the tail region from Ge2021

$$\frac{dN_e}{dE_e} = N_{0,e} \left(\frac{E_e}{1 \text{ TeV}} \right)^{-\alpha_e} \left[1 + \left(\frac{E_e}{E_{e,b}} \right)^\sigma \right]^{-\frac{\Delta\alpha_e}{\sigma}} e^{-\left(\frac{E_e}{E_{e,\max}} \right)^2}, \quad (1)$$

where $\alpha_e = 2.3$ is the spectral index before the break, $\Delta\alpha_e = 1.4$ is the index change when the energy exceeds the break energy $E_{e,b} = 5 \text{ MeV}$, $\sigma = 5$ is the smoothness of the spectral break, and $E_{e,\max} = 200 \text{ TeV}$ is the cutoff energy. $N_{0,e}$ is a normalization factor determined by $\int E_e \frac{dN_e}{dE_e} dE_e = W_e$, where the total energy W_e is obtained by fitting the data, and the limit of integration is from 5 MeV to 5 PeV. They use a $B = 20 \mu\text{G}$ magnetic field and $W_e = 3 \times 10^{46} \text{ erg}$. To highlight the difference between the dominant positions of the two kinds of electrons, we introduce a truncated angular distance θ_c with the intensity of the SNR multiplied by a factor $e^{-\theta_c/\theta}$.

For PWN-originated electrons, the temporal evolution with spin-down history taken into account is considered since the pulsar's birth. The injection rate is written as

$$Q_{\text{inj}}(E_e, t) \equiv \frac{dN}{dE_e dt} = Q_0(t) \left(\frac{E_e}{1 \text{ TeV}} \right)^{-p} e^{-\frac{E_e}{E_{\text{cut}}}}, \quad (2)$$

where p is the injection spectral index, and E_{cut} is the cutoff energy. The normalization factor $Q_0(t)$ is determined by $\int E_e Q_{\text{inj}}(E_e, t) dE_e = \eta_e L_t(t)$, where η_e is the energy conversion efficiency. We consider spherical propagation with the pulsar being the injection point source and neglect the proper motion of the pulsar for simplicity. To avoid superluminal propagation, the generalized Jüttner function (16) is adopted to consider both ballistic and diffusive mechanisms, i.e.,

$$P_J(E_e, r, t) = \frac{H(ct - r)}{4\pi(ct)^3} \frac{1}{\left[1 - \left(\frac{r}{ct} \right)^2 \right]^2} \frac{y(E_e, t)}{K_1[y(E_e, t)]} \exp \left[-\frac{y(E_e, t)}{\sqrt{1 - \left(\frac{r}{ct} \right)^2}} \right], \quad (3)$$

Parameter	p	B (μG)	D_0 ($\text{cm}^2 \text{s}^{-1}$)	δ	η_e	θ_c (arcsec)
range	[1, 3]	[1, 10^3]	[10^{25} , 10^{30}]	[0, 1]	[10^{-6} , 1]	[10, 10^3]
value ($\pm 1\sigma$)	$2.1^{+0.13}_{-0.18}$	142^{+22}_{-22}	$1.5^{+1.1}_{-0.68} \times 10^{29}$	$0.56^{+0.30}_{-0.36}$	$3.8^{+5.2}_{-2.1} \times 10^{-4}$	75^{+99}_{-50}

Table 1: First row: model parameters; second row: searching range of parameters; third row: best-fit values and 1σ uncertainties. Among the six parameters, B , D_0 , η_e and θ_c take the logarithm in MCMC.

where $y(E_e, t) = \frac{c^2 t^2}{2\lambda(E_e, t)}$, and $\lambda(E_e, t) = \int_t^{t_{age}} D[E'_e(t')] dt'$. $H(x)$ is the Heaviside function, $K_1(x)$ is the first-order modified Bessel function of the second kind, and $E'_e(t')$ describes the change of electron energy over time. The energy loss of the electrons is given by (17)

$$\dot{E}_e = -\frac{4}{3}\sigma_T c \left(\frac{E_e}{m_e c^2}\right)^2 \left\{ U_B + \sum_i U_{\text{ph},i} / \left[1 + \left(\frac{2.82kT_i E_e}{m_e^2 c^4}\right)^{0.6} \right]^{\frac{1.9}{0.6}} \right\}, \quad (4)$$

where σ_T is the Thomson cross-section, m_e is the mass of the electron, c is the speed of light, and k is the Boltzmann constant. $U_B = B^2/8\pi$ is the magnetic field energy density, and $U_{\text{ph},i}$ and T_i are the radiation field energy density and the corresponding temperature of the i th component, respectively (see Table 1 in Liang et al. (18), the published paper). Combining Equations 2, 3 and 4, the electron distribution at t_{age} can be expressed as

$$N(E_e, r) = \int_0^{t_{age}} Q_{\text{inj}}(E_g, t) P_J(E_e, r, t) \frac{dE_g}{dE_e} dt, \quad (5)$$

where E_e is the electron energy at the moment, and E_g is the initial energy of the electron injected at time t . It is worth noting that the distribution of relativistic electrons is no longer angular symmetric due to the introduction of ballistic propagation and is calculated following Prosekin et al (19).

We have six free parameters in total: the injection spectral index p , the magnetic field B , D_0 and δ from the energy-dependent diffusion coefficient $D(E) = D_0 (E_e/100 \text{ TeV})^\delta$, the injection efficiency η_e and the truncated angular distance θ_c . Other fixed parameters are listed in Table 2 in (18). The range of the six free parameters and the best-fit result with 1σ from MCMC are listed in Table 1. We put the best-fit values into the model and obtain the fitting radial profiles in Figure 2, resembling Figure 3A from Ge2021. The fitting curve in Figure 2 can well reproduce the two profiles simultaneously. In the relatively strong magnetic field $B = 142 \mu\text{G}$, U_B reaches about $500 \text{ eV}/\text{cm}^3$ and is much larger than U_{ph} . The IC scattering of electrons is severely suppressed and high-energy gamma-ray photons are thus difficult to be produced by PWN-accelerated electrons. Therefore, the Boomerang nebula cannot be a leptonic PeVatron.

Although the fitting result is fairly good, there are some limited aspects. First, we simply adopt a homogeneous magnetic field and diffusion coefficient in the model. A more complete conclusion will be reached if variations are taken into account. Second, we only consider diffusive transport of particles in the PWN, but other transport mechanisms such as advection may also play an important role in the electron distribution (e.g., (20–22)). Last, the isotropic propagation may be a simplification considering the irregular shape of Boomerang, and the reverse shock generated by the dense clouds in the northeast may also affect the particle acceleration and propagation.

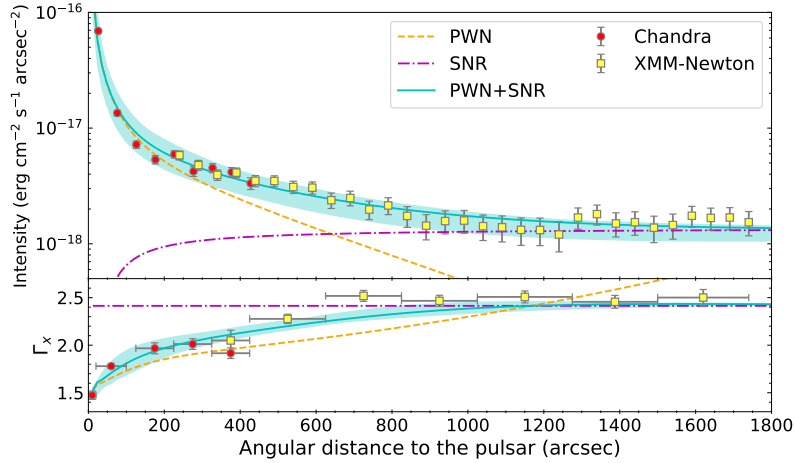


Figure 2: The fitting result of the radial profiles of X-ray surface brightness and photon index. The orange dashed line represents the PWN electron component, the purple dash-dotted line represents the SNR electron component, and the cyan solid line with a 1σ error band is the sum of the two. Red and yellow data points are from Chandra and XMM-Newton, respectively, taken from Ge2021. Only statistic errors are shown.

3. Energy Spectra

LHAASO detected significant signals of UHE photons well above 100 TeV in this PWN-SNR complex, and the angular extension of the UHE emission covers part of the head region. Therefore, the possibility of part of the UHE emission originating from Boomerang cannot be completely excluded. We try to fit the multi-wavelength energy spectrum with the previously obtained best-fit magnetic field $B = 142 \mu\text{G}$, envisaging that a second spectral component may also exist in Boomerang and could possibly account for part of the UHE emission. The first electron component,

$$\frac{dN_e}{dE_e} = N_{0,e} \left(\frac{E_e}{1 \text{ TeV}} \right)^{-\alpha_e} e^{-\frac{E_e}{E_{e,\text{cut}}}}, \quad (6)$$

accounts for the X-ray emission. We add an electron component (i.e., the two-component leptonic scenario) or a proton component (i.e., the lepto-hadronic scenario) as the second component, whose emission is set to contribute half of the measured flux at 500 TeV by LHAASO.

In the former scenario, the second electron component is assumed to follow the Maxwellian distribution (23), i.e.,

$$\frac{dN_m}{dE_m} = N_{0,m} \left(\frac{E_m}{1 \text{ TeV}} \right)^2 e^{-\frac{E_m}{E_{m,\text{cut}}}}. \quad (7)$$

The generated energy spectrum is shown in the left panel of Figure 3. Remarkably, the synchrotron radiation of the Maxwellian type forms a significant bump in the MeV band, which has a much higher flux and harder spectrum compared to the measurement from both Chandra and NuSTAR, making this scenario unlikely to be realistic. An even narrower distribution than the Maxwellian for the spectrum of the second electron component can be invoked to avoid the X-ray constraints, but its formation mechanism is unclear.

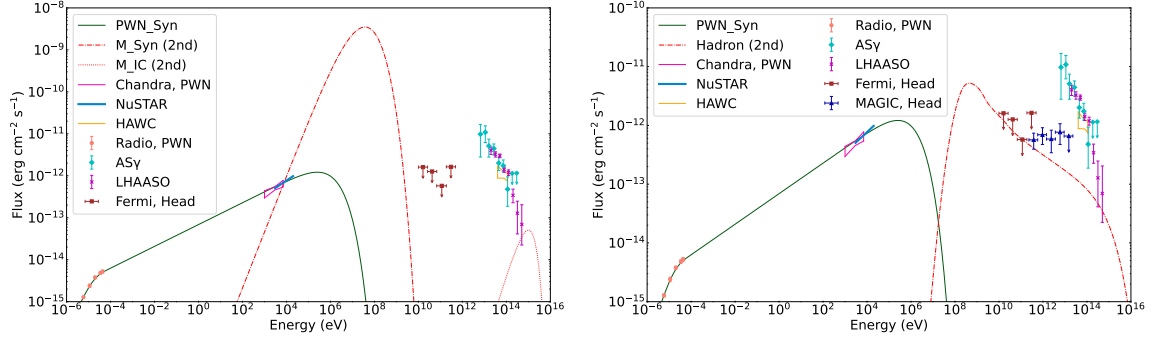


Figure 3: **Left panel:** The two-component leptonic scenario for the head region. The dark green solid line is the synchrotron radiation of the power-law type electrons, and the red dash–dotted and dotted lines are the synchrotron and IC radiation of the Maxwellian-type electrons, respectively. The salmon points on the left are the radio data (24), and the bright pink butterfly plot is from the observation of Chandra in Ge2021. The recent NuSTAR measurement at 3–20 keV is also shown in cerulean (25). The brown upper limit of the GeV band comes from of the head region by Fermi-LAT (26), while the cyan and magenta TeV data points and orange butterfly plot on the right are from AS γ (14), LHAASO (1), and HAWC (13), respectively. The GeV–TeV observations are shown for reference and not involved in the fitting, since most of them are spatially coincident with the tail region. **Right panel:** The leptohadronic scenario. The dark green solid line represents the synchrotron radiation of electrons, and the red dash–dotted line represents gamma-ray radiation from π^0 decay. The MAGIC data from the head region in royal blue are shown for reference.

1st e (Equation (6))	α_e 2.5	$E_{e, \text{cut}}$ (eV) 4.0×10^{14}	$E_{e, \text{min}}$ (eV) 1.0×10^9	W_e (erg) 1.3×10^{43}
2nd e (Equation (7))	$E_{m, \text{cut}}$ (eV) 4.0×10^{14}	$E_{m, \text{min}}$ (eV) 1.0×10^{12}	W_m (erg) 7.5×10^{42}	
p (Equation (8))	α_p 2.4	$E_{p, \text{cut}}$ (eV) 1.0×10^{16}	W_p (erg) 1.3×10^{48}	n_{gas} (cm^{-3}) 10

Table 2: Fitting parameters of the two-component leptonic scenario and leptohadronic scenario, corresponding to Figure 3. The former comprises the PWN electron component (first row) plus the Maxwellian type (second row), and the latter comprises the PWN electron component plus proton component (third row).

As for the leptohadronic scenario, the additional proton component is given by

$$\frac{dN_p}{dE_p} = N_{0, p} \left(\frac{E_p}{1 \text{ TeV}} \right)^{-\alpha_p} e^{-\frac{E_p}{E_{p, \text{cut}}}}. \quad (8)$$

We calculate the pionic gamma-ray spectrum generated by the proton–proton collisions (27), and the resultant gamma-ray emission remains high at 1 PeV before dropping. The proton spectrum index is not well constrained, and we show a steep spectrum approaching the upper limit of Fermi-LAT in the right panel of Figure 3. The total energy of the protons is inversely proportional to the gas density, while the latter takes a hypothetical value here. If we try to fit the 500 TeV point and the MAGIC data (11) at the same time, a flatter injection spectrum with lower cutoff energy and less total energy would be expected. Assuming the moment of inertia of the pulsar to be 10^{45} g cm^2 , the total spin-down energy dissipated since its birth is $4.9 \times 10^{48} \text{ erg}$, according to $E_{\text{rot}} = \frac{1}{2} I (2\pi/P)^2$. It is greater than the sum of the energies of the electron and proton, so the scenario does not violate the

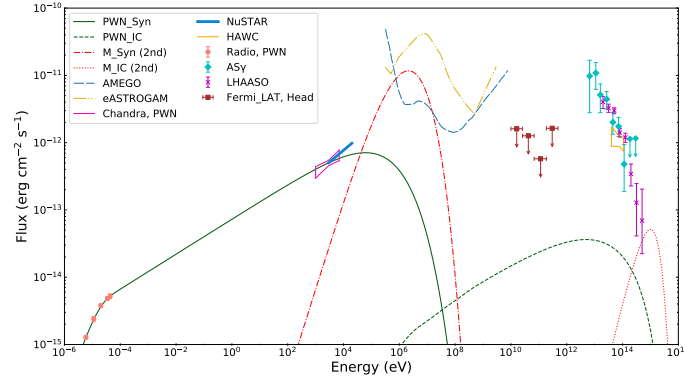


Figure 4: The two-component leptonic scenario with magnetic field obtained from Hillas condition. The dark green solid and dashed lines are the synchrotron and IC radiation of the power-law type electrons, respectively, and the red dash-dotted and dotted lines are the synchrotron and IC radiation of the Maxwellian-type electrons, respectively. The gold dash-dot-dotted curve and the blue dashed curve show the 1 Ms sensitivity of the next-generation MeV gamma-ray detectors e-ASTROGAM (30) and AMEGO (31), respectively. Observation data are the same as the ones in Figure 3.

α_1	$E_{1,\text{cut}} \text{ (eV)}$	$E_{1,\text{min}} \text{ (eV)}$	$W_1 \text{ (erg)}$	$E_{2,\text{cut}} \text{ (eV)}$	$E_{2,\text{min}} \text{ (eV)}$	$W_2 \text{ (erg)}$
2.5	7.6×10^{14}	4.4×10^9	9.6×10^{44}	4.0×10^{14}	1.0×10^{12}	7.5×10^{42}

Table 3: Fitting parameters of the two-component leptonic scenario with a relatively weaker magnetic field, corresponding to Figure 4.

energy conservation. Therefore, if the future observations reveal that part of the UHE gamma-ray emission arises from the Boomerang Nebula, our analysis will indicate that it is a hadronic PeVatron.

At last, we examine the result from another perspective. If the electrons from the PWN can substantially contribute to the UHE gamma-ray emission, a weaker magnetic field will be required. Thus, we estimate the weakest possible magnetic field and ignore the constraint from X-ray profiles. The Hillas condition (28) requires $B \gtrsim E_e/eR$, where R corresponds to the termination shock radius of about 0.1 pc with a reference to the Crab (17, 29). The emitted gamma-ray photon energy via the IC mechanism can be estimated via $E_{\text{IC}} \sim E_e \Gamma / (1 + \Gamma)$, where $\Gamma = \gamma \epsilon / mc^2$ with $\epsilon = 2.82kT$ being the average photon energy of the black body radiation. To scatter CMB photons up to $E_{\text{IC}} = 500$ TeV, the corresponding electron energy needs to be $E_e \approx 760$ TeV. Therefore, the Hillas condition gives a lower limit of magnetic field $B_{\text{H,LL}} = 8.2 \mu\text{G}$. Similar to the two-component leptonic scenario described above, we fit the SED shown in Figure 4 using $B_{\text{H,LL}}$ and other parameters listed in Table 3. In the weakest possible magnetic field, the IC flux from the first electron component is still far less than the measured values. Again, if we attribute half the 500 TeV flux to the second electron component, a prominent synchrotron bump peaking at the MeV regime will still be expected. It is not in contrast with the current X-ray observation, and the next-generation MeV gamma-ray instruments such as e-ASTROGAM (30) and AMEGO (31) will be helpful to discern.

References

1. Z. Cao *et al.*, *Nature* **594**, 33–36 (June 2021).

2. S. Pineault, G. Joncas, *AJ* **120**, 3218–3225 (Dec. 2000).
3. R. Kothes, B. Uyaniker, S. Pineault, *ApJ* **560**, 236–243 (Oct. 2001).
4. Q.-C. Liu, P. Zhou, Y. Chen, *ApJ* **926**, 124 (Feb. 2022).
5. C. Ge, R.-Y. Liu, S. Niu, Y. Chen, X.-Y. Wang, *The Innovation* **2**, 100118 (May 2021).
6. Y. Bao, Y. Chen, *ApJ* **919**, 32 (Sept. 2021).
7. Y. Xin, H. Zeng, S. Liu, Y. Fan, D. Wei, *ApJ* **885**, 162 (Nov. 2019).
8. K. Fang, M. Kerr, R. Blandford, H. Fleischhack, E. Charles, *PRL* **129**, 071101 (Aug. 2022).
9. A. A. Abdo *et al.*, *ApJL* **664**, L91–L94 (Aug. 2007).
10. A. A. Abdo *et al.*, *ApJL* **700**, L127–L131 (Aug. 2009).
11. MAGIC Collaboration *et al.*, *A&A* **671**, A12 (Mar. 2023).
12. V. A. Acciari *et al.*, *ApJL* **703**, L6–L9 (Sept. 2009).
13. A. Albert *et al.*, *ApJL* **896**, L29 (June 2020).
14. Tibet ASy Collaboration *et al.*, *Nature Astronomy* **5**, 460–464 (Jan. 2021).
15. Y. Fujita, A. Bamba, K. K. Nobukawa, H. Matsumoto, *ApJ* **912**, 133 (May 2021).
16. R. Aloisio, V. Berezhinsky, A. Gazizov, *ApJ* **693**, 1275–1282 (Mar. 2009).
17. LHAASO Collaboration *et al.*, *Science* **373**, 425–430 (July 2021).
18. X.-H. Liang, C.-M. Li, Q.-Z. Wu, J.-S. Pan, R.-Y. Liu, *Universe* **8**, 547 (Oct. 2022).
19. A. Y. Prosekin, S. R. Kelner, F. A. Aharonian, *PRD* **92**, 083003 (Oct. 2015).
20. C. F. Kennel, F. V. Coroniti, *ApJ* **283**, 710–730 (Aug. 1984).
21. A. Van Etten, R. W. Romani, *ApJ* **742**, 62 (Dec. 2011).
22. W. Ishizaki, K. Asano, K. Kawaguchi, *ApJ* **867**, 141 (Nov. 2018).
23. F. A. Aharonian, A. M. Atoyan, presented at the Neutron Stars and Pulsars: Thirty Years after the Discovery, ed. by N. Shibasaki, p. 439.
24. R. Kothes, W. Reich, B. Uyaniker, *ApJ* **638**, 225–233 (Feb. 2006).
25. K. Mori *et al.*, presented at the 37th International Cosmic Ray Conference. 12-23 July 2021. Berlin, 963, p. 963.
26. S. Liu, H. Zeng, Y. Xin, H. Zhu, *ApJL* **897**, L34 (July 2020).
27. E. Kafexhiu, F. Aharonian, A. M. Taylor, G. S. Vila, *PRD* **90**, 123014 (Dec. 2014).
28. A. M. Hillas, *ARA&A* **22**, 425–444 (Jan. 1984).
29. B. M. Gaensler, P. O. Slane, *ARA&A* **44**, 17–47 (Sept. 2006).
30. A. De Angelis *et al.*, *Experimental Astronomy* **44**, 25–82 (Oct. 2017).
31. A. Moiseev, AMEGO Team, presented at the 35th International Cosmic Ray Conference (ICRC2017), vol. 301, 798, p. 798.